Editors' Suggestion | Featured in Physics

Flow and mixing induced by single, colinear, and colliding contractile waves in the intestine

Richard J. Amedzrovi Agbesi* and Nicolas R. Chevalier†
Laboratoire Matière et Systèmes Complexes UMR 7057/ Université Paris Cité, 10 Rue Alice Domon et Léonie Duquet, 75013 Paris, France

(Received 11 November 2021; accepted 16 March 2022; published 15 April 2022)

Smooth muscle-lined organs like the gut, the ureter, and the fallopian tubes transport matter by generating traveling contractile waves. Intestinal peristalsis is characterized by rhythmic trains of shallow, low-amplitude myogenic waves and high-amplitude, lumen-obliterating neurogenic waves. In this paper, we develop a simple analytical Poiseuille-flow model to predict the flow rates induced by these different contractions as a function of all relevant wave parameters, and compare them to a numerical fluid-solid finite element model. We rationalize experimentally observed bolus to-and-fro motion induced by shallow myogenic waves. We show that occluding waves induce considerable bolus mixing due to an upstream vortex. We then investigate the hydrodynamics induced by two waves propagating either in the same direction (colinear) or in opposite directions, as happens in the digestive tract. For colinear waves, we find that the bolus reflux is maximal at a distance between successive myogenic waves close to the one observed physiologically. Colliding waves create a high pressure region that gives rise to rapid fluid flow, high shear stress, and radial mixing upon annihilation. Our paper provides fundamental insight on the fluid dynamics (reflux, propulsion, and mixing) generated by different contraction patterns of the intestine.

DOI: 10.1103/PhysRevFluids.7.043101

I. INTRODUCTION

The gut is a flexible tube through which chyme is propelled and mixed by varying patterns of contraction. The motor activity (peristalsis) of the gut is critical for life [1]. First, it promotes mixing and transfer of nutrients to the wall of the gut for absorption. Second, it must allow the sequential flow of its contents. Peristalsis is based on alternating compression and relaxation of the gut wall, drawing contents in and propelling them away. Peristalsis is one of the primary physiological mechanisms for the transport of fluids from one site to another in the human body. Some examples are the transport of the embryo after fertilization from the fallopian tube to the uterine cavity [2], the passage of urine from the kidneys to the bladder [3], the movement of chyme in the gastrointestinal tract [4–7], and of the food bolus through the oesophagus [8]. Depending on the organ and its functions, different peristaltic wave patterns are developed. The ureter, for example, is a 30-cm long collapsible tube with a diameter of a few millimeters when distended. The human ureter produces successive waves with a period of 10–60 s and a speed of contraction 20–30 cm/s [3]. The contractile wave almost completely obliterates the lumen pushing ahead urine [9]. Because mixing is not necessary in the ureter, contractile waves move in one direction from the upper end to the lower end of the ureter (except in pathological cases). Peristaltic waves in the oesophagus also produce a lumen-occluding

*richard-junior.amedzrovi-agbesi@parisdescartes.fr
†nicolas.chevalier@paris7.jussieu.fr

contraction at a speed of 2.5–5 cm/s [10]. The gut is the longest organ of the body with a length of about 8 m in humans. Unlike the oesophagus and the ureter, the gut ensures efficient mixing of its content. Intestinal peristalsis is characterized by myogenic and neurogenic waves. Myogenic waves, also called slow waves, are rhythmic trains of shallow, low-amplitude smooth muscle contractions that occur independently of any enteric neuronal activity. Myogenic waves are triggered by the rhythmic electric depolarisation of pacemaker cells in the muscle coat, the interstitial cells of Cajal. Neurogenic waves are high-amplitude, lumen-obliterating waves that are triggered and amplified by the secretion of neurotransmitters from the enteric nervous system to the muscle coat [11]. Myogenic and neurogenic waves can both be triggered by mechanical stimulation, for example, by pressure applied by bolus on the gut wall. Contractile waves in the gut can travel in both directions; this bidirectionality (counterpropagating waves) is prominent in the myogenic motor pattern called segmentation [12] that results in bolus mixing without net propulsion. The diversity of contractile patterns gives rise to distinct hydrodynamic flow patterns, which we will decipher in this paper. Early researchers developed analytical models that described the fluctuations in pressure and shear stress, retrograde motion, and the degree of tube occlusion on global pumping performance for a peristaltic tube [13,14]. Recent studies have investigated the effects of propagating coordinated circular and longitudinal contractions on mixing and propulsion [5,6]. Much data has been provided as to the significant role played by segmentation (nonpropagating circular contraction) and pendular movements (nonpropagating longitudinal contraction) on mixing [4,6,15]. Finite element models (FEMs) have shown that a zone of stasis without vortical motion appears downstream of the point of constriction, whereas a transient region of vortical flow forms upstream [7]. Other works have looked at intestinal mixing of digesta with varying rheological properties using FEMs [6,7]. Sinnot modeled the descending inhibition that causes relaxation of the gut using smooth particle hydrodynamics and showed that it improves mixing and transport [16].

Flow characteristics described by most studies are based on a single peristaltic wave. Interestingly, the gut produces several periodic waves (train waves) that either travel in the same direction (colinear waves) or in opposite directions. When waves traveling in opposite directions collide, they annihilate [17]. Not very much is known about train and colliding waves and the role they play depending on their wave amplitude and spacing distance. Early work done on train waves showed that it induces less reflux than single waves [13]. It has also been hypothesized that train waves will be more effective at continuous pumping than widely spaced peristaltic waves [13]. Experimental studies have been carried out by Refs. [5,18,19] to quantify mixing by longitudinal and circumferential contractions using residence time analysis. A recent study has quantified mixing and its dependence on circular folds with varying segmentation amplitude, frequency, and velocity by numerical simulations [20].

Here, we start by presenting basic experimental features of contractile wave propagation in the gut: the to-and-fro bolus displacement induced by colinear waves and the local rapid fluid-flow induced by colliding waves. We then develop a simple Poiseuille analytical model to predict fluid flow and pressure profiles for a single propagating wave as a function of all relevant parameters: wave speed, amplitude, length, and bolus viscosity. We next compare this analytical model with a numerical FEM and rationalize the experimentally observed bolus trajectories. We extend this numerical model to the case of two colinear or colliding waves. We finally examine the mixing, absorption, and propulsion capacity of the different contraction patterns and discuss why different organs (gut, ureter, oesophagus) adopt different wave patterns.

II. METHODOLOGY

A. Experimental model

We examined displacements of meconium (naturally present, dark liquid bolus) or silicone oil (injected, light bolus) in isolated 18.5-day-old embryonic (E18.5) C57B6 (Mus musculus) mice hindgut and 13-day-old (E13) chicken embryonic midgut. Both exhibit purely myogenic

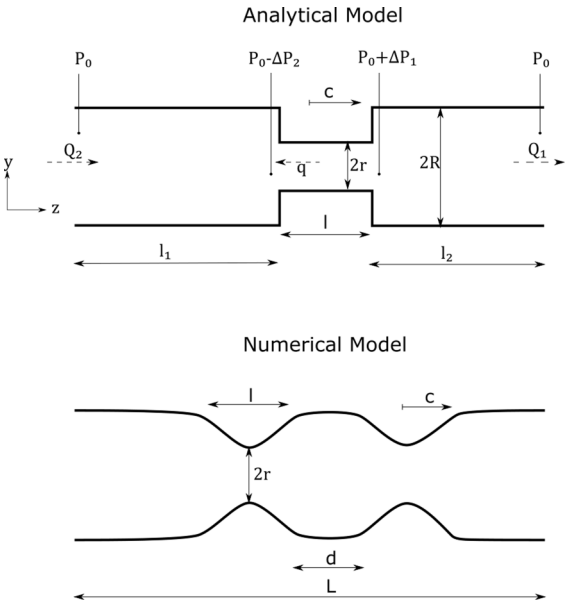

FIG. 1. Geometry of the analytical and numerical models. A gut under the effect of a single wave. c is the velocity of the wave, l is the length of the wave, P is the pressure, Q is the out inflow/outflow rate, q is the retrograde flow induced by the traveling wave, R is the radius of the the gut, r is the radius of the occluded segment ($r = 0$ complete occlusion).

(nonneurogenic) [21] motility at these stages [22]. The experimental set-up (see the full setup, Fig. S2, in the Supplemental Material [23]) has been previously described [24]; it consisted of a trough filled with Dulbecco's Modified Eagle Medium (DMEM) at 37 °C and continuously bubbled with 95% O_2–5% CO_2. The whole gut was pinned vertically to one wall of the trough, and gut and bolus motion (See the movie, video S1, in the Supplemental Material [23]) recorded by 3 Hz time-lapse imaging with a Stingray 1600 x 1200 px camera equipped with a Computar x0.8-x3.2 lens. Bolus and contractile wave velocities were derived from spatiotemporal maps [Fig. 2(b)] generated with the ImageJ reslice function as previously described [25]. The occlusion ratio(amplitude of contraction) of the wave was measured directly from the video as

$$A = 1 - \frac{2r}{2R}. \tag{1}$$

r and R are defined in Fig. 1.

B. Numerical method-single peristaltic wave

We employed COMSOL Multiphysics combined structural mechanics (tube deformation) and fluid dynamics finite-element package. Since the intestine is tubular, we used a 2D axisymmetric model as outlined in Fig. 1(b). The thickness of the wall was taken as 5% of the total radius R of the tube. To model wall contraction, a time-dependent, traveling Gaussian-shaped force density is applied to the outer wall of the tube, in the radial direction, and is independent of the fluid properties. The pressure applied was 0.1 to 0.25 (nondimensionalized by the Young modulus of the tube material used) to create, respectively, a 25% to 88% occlusion ratio. Contraction initiation was obtained by multiplying the force density by a smoothed Heaviside function which kicks in at $t = 0.3$ s and takes the force to its full development at $t = 0.5$ s; after fluid dynamics reached a stationary state in the reference frame of the wave, the contraction was damped back to zero between 8.8 s and 9 s. For the structural mechanics part, we assumed that the gut wall was a linearly elastic

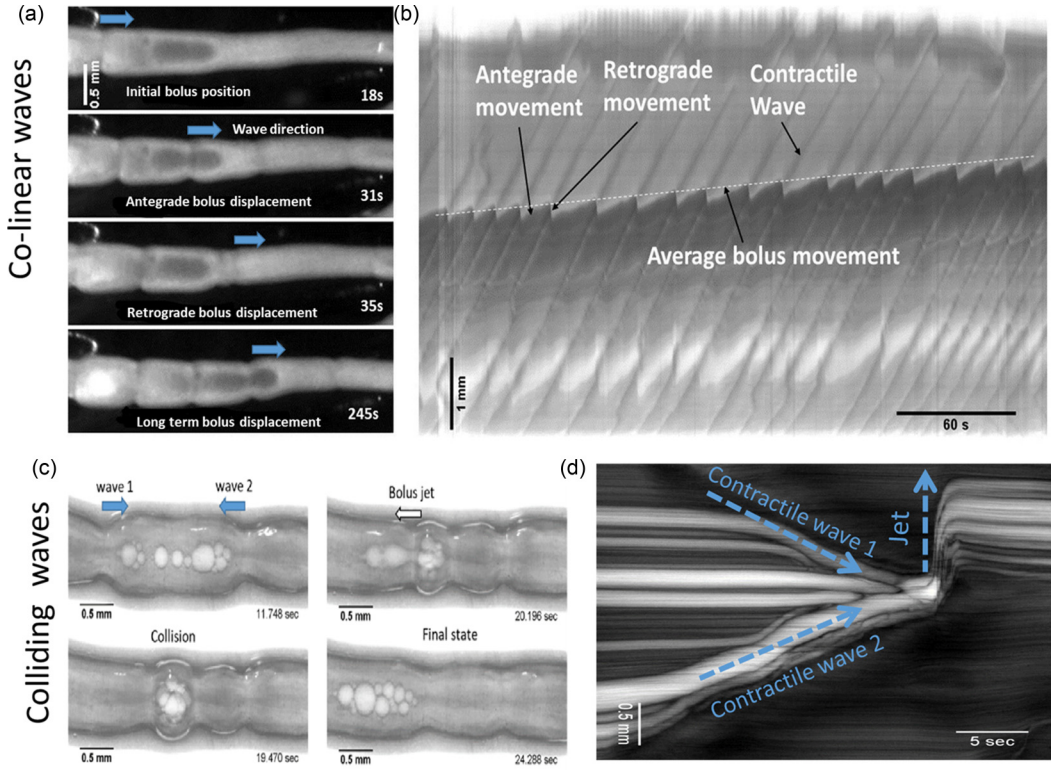

FIG. 2. Experimental bolus dynamics. (a) Colinear waves moving from left to right and displacing dark bolus (meconium), initial position, antegrade propulsion, reflux, and bolus displacement after 4 min. Frames selected from video S1 [23]. (b) Space-time diagram of bolus (dark grey) and contractile wave (light grey) dynamics from video S1 [23]. (c) Counterpropagating waves concentrate the bolus (silicone oil) to one point, creating a high-pressure area at the collision point with subsequent high-velocity jet formation (here toward the left). Frames selected from video S2 [23]. (d) Space-time diagram of bolus displacement by contractile waves and rapid jetting after wave collision, from video S2 [23].

material. The outer surface of the tube was free to move and deform, while the inlet and outlet of the tube were fixed along the z and y coordinate axes. The mesh was fixed to a zero y displacement on the symmetry axis and a zero z displacement at the inlet and outlet of the tube. For the fluid simulations, we assumed a no-slip condition between the wall of the tube and the fluid, and that the fluid cannot penetrate through the wall of the tube. We also assumed a zero stress condition at the inlet and outlet.

Because the Reynolds number of bolus flow in the Gastrointestinal tract (GI) are low (Re $<<$ 1), Wormesley's number ($W < 0$), and the lumen radius much smaller than its length (see the rheological properties of the gastrointestinal tract, Table S1, in the Supplemental Material [23]), we used the Navier-Stokes equations with creep assumption:

$$\nabla p = \eta \nabla^2 \mathbf{u}, \tag{2}$$

$$\nabla \cdot \mathbf{u} = 0, \tag{3}$$

where ρ is the density, u the velocity vector, p is the pressure, and η is the viscosity. The equations are solved on an axisymmetric, freely moving, deformed mesh inside the tube. Deformation

of the mesh relative to the initial shape of the domain is computed using Yeoh smoothing [26] and follows the deformation of the tube.

We defined the flow rate at any point z along the tube $Q(z) = \int_{s_r} (\mathbf{u}.\hat{z})ds$, where $\hat{z}$ is the unit vector pointing along z, $\mathbf{u}$ equals the velocity vector, $s(r)$ is the local tube section area.

We followed the movement of a particle using the particle trajectory model in COMSOL multiphysics. A particle of diameter $r = 0.5\ \mu$m and density $=1000\ \mathrm{kg/m^3}$ was placed in the lumen on the z axis. The Stokes drag F_d acting on this particle is

$$F_d = 6\pi r\eta(u - v), \tag{4}$$

where v and u are, respectively, the particle and fluid velocity. The particle is considered small enough not to perturb the velocity field u calculated in the absence of the particle.

We studied the role of several wave patterns (counterpropagating waves, single propagating waves, and colinear train waves) and visualized their effect using 2D axisymmetric transport of diluted species model of COMSOL. A gut model (Fig. 1) is filled with a solute of an initial concentration given by the function

$$\exp\left[\frac{-(r-k)^2}{2q^2}\right], \tag{5}$$

where k is the mean and q is the standard deviation. The function creates a solute gradient from the axisymmetric line to the wall of the gut. The initial concentration gradient is such that it is maximum at the axisymmetric line and decreases to a value of zero at the wall of the gut. We applied periodic boundary conditions at the ends of the tube (inlet and outlet). We imported velocity profile values from the fluid-structure interaction model as the convection input to the transport of diluted species model. We used a diffusion coefficient of $10^{-9}\mathrm{m^2s^{-1}}$ and Peclet number of 5000 because we were interested in estimating mixing as a result of the wave patterns. We quantified absorption by estimating normal convective flux at the wall of the gut.

III. RESULTS

A. Experimental bolus dynamics

Figures 2(a) and 2(b) and video S1 [23] show representative experimental bolus dynamics for colinear waves. They consist of successive, rhythmic (∼4 cycles per minute in this example), radial constrictions of the hindgut wall that propagate in the same direction [from left to right in Fig. 2(a), at a speed of $\sim 74\ \mu$m/s and amplitude of ∼50% in this example] . As a contractile wave approaches the bolus, it pushes it in the direction of the wave [antegrade movement, Fig. 2(a)] at a low speed ($\sim 20\ \mu$m/s–an average value). As the wave travels over the bolus, the latter is suddenly transported in the opposite direction [retrograde movement, Fig. 2(a)], at a much higher speed ($\sim 220\ \mu$m/s–an average value). After the wave passes the bolus, the latter continues traveling slowly in the antegrade direction, at the speed of $20\ \mu$m/s. This cycle repeats itself with each successive wave, giving rise to a characteristic sawtooth pattern of bolus displacement [Fig. 2(b)]. A net, long-term antegrade (left to right) bolus displacement is conspicuous after several cycles [Figs. 2(a) and 2(b), long-term bolus displacement]; in this particular example, we measure a speed $\sim 2\ \mu$m/sec. Four characteristic speeds emerge from these preliminary observations: the speed of the contractile wave, the antegrade and retrograde bolus speeds for one cycle, and the long-term (cycle-averaged) antegrade bolus speed.

Figures 2(c) and 2(d) and video S2 (see Supplemental Material [23]) show representative experimental bolus dynamics for colliding waves. In this case, the bolus is artificially injected silicone oil because the size of the droplets is bigger than that of the occlusion; they are shoved toward the center by the contractile waves, at the same speed as the contractile waves (0.1 mm/s). When the waves collide, they create a local high-pressure region, from which a high-speed jet of bolus emerges (toward the left, at a speed of 3.3 mm/s).

Following these observations, the general questions we ask are the following: Given all characteristics of the contractile waves, can we quantitatively predict the velocity and to-and-fro motion of the bolus? Does bolus viscosity matter? Does the effect of successive, colinear contractile waves simply sum up or do their flow patterns interact? What pressures and resulting jet speeds are generated upon counterpropagating wave collision? Do these different wave patterns induce mixing?

B. Analytical method-single peristaltic wave

First, we devised a simple analytical model based on Poiseuille's law to model the flow induced by propagating contractile waves. Muscle contraction induces a wave over a length l, a reduction of lumen size from a value at rest R to a constricted value $r < R$, as shown in Fig. 1; this constriction propagates from left to right at a speed c. The propagating contraction induces a net forward volume flow Q, an increased pressure $P_0 + \Delta P_1$ downstream of the contraction, a decreased pressure $P_0 - \Delta P_2$ upstream, and a backward volume flow q inside the constricted lumen as a result of this pressure differential. Applying Poiseuille's law to the three different segments of the gut yields

$$\Delta P_1 = \frac{8\eta l_1 Q_1}{\pi R^4}, \tag{6}$$

$$\Delta P_2 = \frac{8\eta l_2 Q_2}{\pi R^4}, \tag{7}$$

$$\Delta P_1 + \Delta P_2 = \frac{8\eta l q}{\pi r^4}, \tag{8}$$

where η is the dynamic viscosity and all other variables are described in Fig. 1(a). Volume conservation implies $c\pi(R-r)^2 = Q + q$ and $Q_1 = Q_2 = Q$. The net flow rate Q induced in a pipe of length $L = l_1 + l_2$ by a rectangular constriction of speed c, length l, and occlusion ratio r/R can then be derived from these considerations:

$$Q = \frac{c\pi(R-r)^2}{\left[1 + \left(\frac{r}{R}\right)^4\left(\frac{L}{l}\right)\right]}. \tag{9}$$

For almost complete occlusion $r/R << 1$, Eq. (9) simplifies to

$$Q = c\pi R^2\left(1 - 2\frac{r}{R}\right). \tag{10}$$

For a wavelength small compared to tube length, $l/L << 1$:

$$Q = \frac{lc\pi R^6}{Lr^4}\left(\frac{r}{R} - 1\right)^2. \tag{11}$$

In the following, we nondimensionalize length, fluid speed, and, consequently, flow by introducing the following variables:

$$\tilde{Q} = \frac{Q}{cR^2}, \quad \tilde{u} = \frac{u}{c}, \quad \tilde{r} = \frac{r}{R}, \quad \tilde{l} = \frac{l}{R}, \tag{12}$$

where u is the velocity field of the fluid inside the gut and c is the velocity of the wave.

C. Single-wave hydrodynamics

Figures 3(a)– 3(c) show the velocity fields obtained for contractile waves of increasing amplitude (12, 25, and 88%). Figure 3(d) shows that the constriction creates a negative pressure upstream and a positive pressure downstream of the constriction in both numerical (FEM) and analytical Poisseuille models. The flow on either side of the contraction is laminar and antegrade [Figs. 3(a)–3(c), and 3(e)], while a reflux flow at the site of the contraction is predicted by both numerical and analytical models [Fig. 3(e)]. We note that both the pressure differential and the axial velocities predicted by the analytical model were one order of magnitude lower than in the numerical case (we explain this

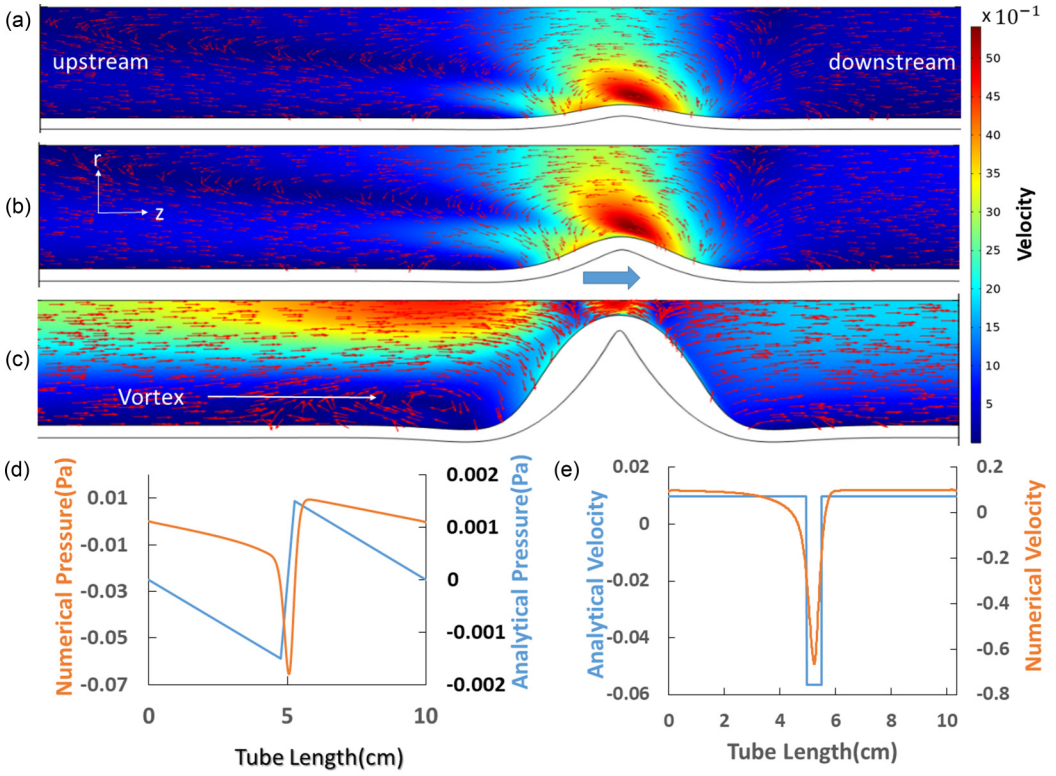

FIG. 3. Numerical and analytical flow and pressure profiles for a single propagating contractile wave. The wave travels from left to right at a velocity of $\tilde{c} = 1$ and the dynamic viscosity is 1×10^{-3} Pa s. (a)–(c) Velocity field for contractile wave of 12%, 25% and 88% amplitude. Velocity is dimensionless according to (12). (d)–(e) Pressure and velocity field for 25% wave amplitude.

discrepancy in the Discussion section). The numerical model further revealed vortical flow at the apex of the contraction at 12% and 25% amplitude [Figs. 3(a) and 3(b)], while the collision of the high velocity reflux jet with the oppositely moving (antegrade) fluid at 88% wave amplitude induces a vortex upstream of the contraction [white arrow, Fig. 3(c)].

We next computed the flow rate $\tilde{Q}$ as a function of the wave length $\tilde{l}$, speed $\tilde{c}$, amplitude $\tilde{A}$, and the viscosity η [Figs. 4(a)–4(d)]. The general trends predicted by the analytical and numerical models were in agreement. Analytical flow rates were always lower than numerical ones, which comes as a result of the lower differential pressures in the analytical case. We found that the flow rate $\tilde{Q}$ increases linearly with the length of wave $\tilde{l}$ [Fig. 4(a)] for $\tilde{l} >> \tilde{L}$ as predicted by Eq. (11), that it increases linearly with wave speed c [Fig. 4(b)] as predicted by Eq. (9), that it increases linearly with wave amplitude for high occlusion [$r/R << 1$, Fig. 4(c)] as predicted by Eq. (10), and that it is independent of viscosity in the range 1–10 mPas Fig. 4(d). For the same force density applied to the wall of the gut with increasing dynamic viscosity, the deformation created decreases above 10 mPas. This explains the nonconstant numerical curve in Fig. 4(d).

D. Single-wave particle trajectory

We next investigated the trajectory of a small particle inside the liquid bolus using our numerical approach. The motion of the particle depends on the relative size of the particle to the amplitude of the wave [Figs. 5(b) and 5(d)]. For shallow waves (constricted lumen diameter is bigger than particle diameter), we found that as the wave approached the particle, the latter first moved in the direction

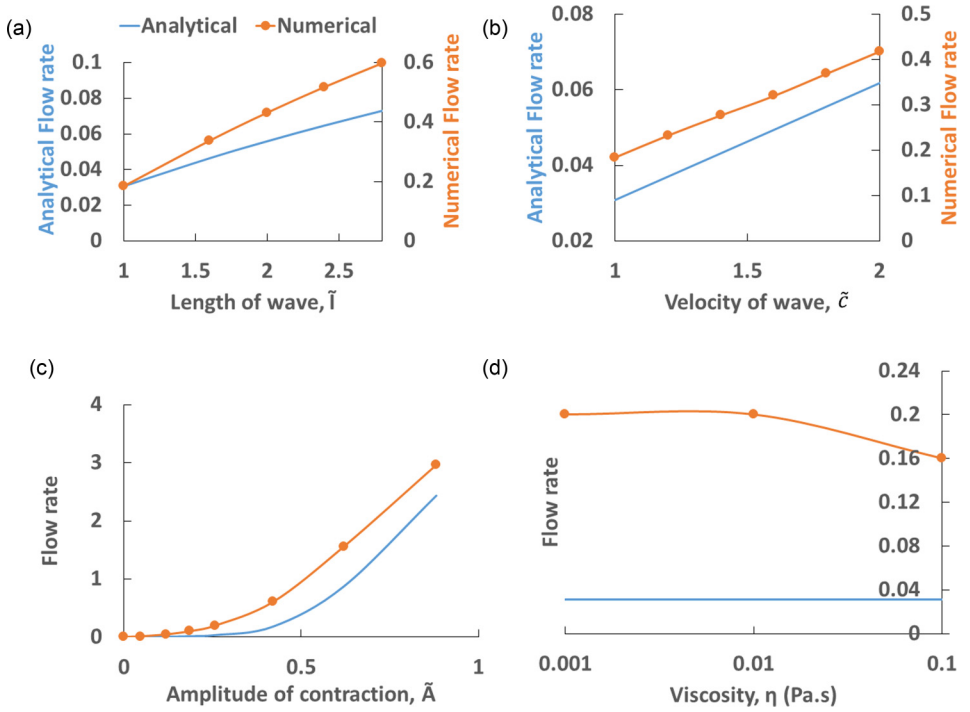

FIG. 4. Flow rate as a function of contractile wave characteristics and bolus viscosity. All values are dimensionless as introduced in Eqs. (12), except for viscosity (Pa s). All parameters but the variable investigated were kept constant: $\tilde{l} = 1$, $L/R = 20$, $\tilde{c} = 1$, 25% amplitude contraction, η=1 $\times$ 10^{-3} Pa s.

of the wave [Figs. 5(a) and 5(b)] with constant velocity. It was then abruptly refluxed in the opposite direction as the wave reached the particle. It finally returned to the constant-speed antegrade motion as the wave moved past it. The total displacement of the particle after one wave cycle was small compared to the length of the tube.

For occluding waves (constricted lumen smaller than particle size), there is no to-and-fro motion and the particle travels in the antegrade direction at the same velocity as the contractile wave [Figs. 5(c) and 5(d)].

E. Multiple wave effects: Colinear waves

We next wondered whether the fact that contractile waves are physiologically generated as trains of successive waves [Fig. 2(a)] could induce collective phenomena that are not captured by the single wave model we developed hitherto. We therefore calculated the flow maps [Figs. 6(a)–6(c)] for two contractile waves as a function of their distance of separation $\tilde{d}$ relative to the radius of the tube R, i.e., $\tilde{d} = d/R$. We found that for an interwave distance $\tilde{d} > 3.2$ [Fig. 6(a)], the two waves could be considered as two noninteracting single waves: the flow pattern in the space between the waves was unidirectional across the whole gut radius and the flow at the outlet of the gut was equal to that generated by two single waves [Fig. 6(e)]. For an intermediate distance of separation $\tilde{d} = 1.2$, the flow pattern [Fig. 6(b)] between the two waves is characterized by the coexistence of retrograde flow (reflux) near the gut axis, and antegrade, vortical flow further away from the axis. When the distance between the two waves is further reduced [$\tilde{d} = 0.2$, Fig. 6(c)], the reflux flow dominates and the region of antegrade vortical flow becomes confined to a small region at the periphery of the lumen; in this case, the flow induced by the two waves roughly sums up to that induced by a single wave with a higher effective wave length. We quantified reflux by measuring the extent of backward displacement of a particle during wave propagation. The displacement value

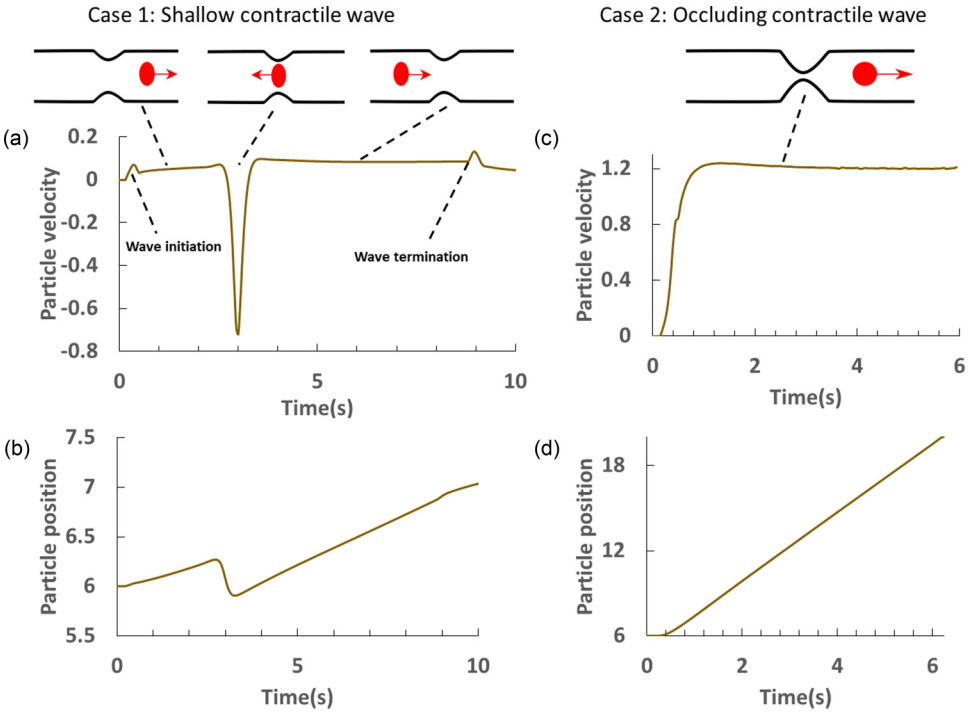

FIG. 5. Particle trajectory for shallow and high-amplitude waves. Velocity and position values are nondimensionalized by the wave velocity and tube diameter respectively. (a), (b) Particle velocity and position along the z axis for a shallow contractile wave (25% of resting amplitude) and (c), (d) for an occluding contractile wave (88% amplitude).

is normalized by the radius of the gut to give the reflux value. We found that reflux is maximal at an interwave separation distance of 1.2 [Fig. 6(d)] and contractile wave amplitude of 40% (see reflux as a function of contraction amplitude, Fig. S1, in the Supplemental Material [23]). Single successive waves ($\tilde{d} > 3.2$) generate about 20% less reflux compared to train waves at $\tilde{d} = 1.2$. We also found that the output flow generated by train waves is a nonlinear function of the distance between waves and is always less than the flow generated by two isolated waves [Fig. 6(e)].

F. Multiple wave effects: Colliding waves

A last motility pattern that is unique to the gastrointestinal tract is that of counterpropagating contractile waves. When two counterpropagating contractile waves meet, they annihilate [27]. We explored the velocity and pressure profiles for counterpropagating waves of low [25%, Figs. 7(a)–7(c)] and high [88%, Figs. 7(e)–7(g)] amplitudes. For high-amplitude waves, the pressure profile was a simple step function, i.e., 0 outside of the interwave region, and a uniform higher pressure between the two waves that increased as they got closer together. The pressure in the region between the two waves reached 0.05 Pa and 60 Pa for 25% and 88% amplitudes, respectively, i.e., a factor 5 and 130 more than for a single traveling wave. These high pressures resulted in high velocity fluid jets exiting the interwave region at velocities of up to 140 times the speed of the contractile wave. Upon wave annihilation, the fluid exhibits dipolelike vorticity in the radial direction, as seen in Figs. 7(c) and 7(g).

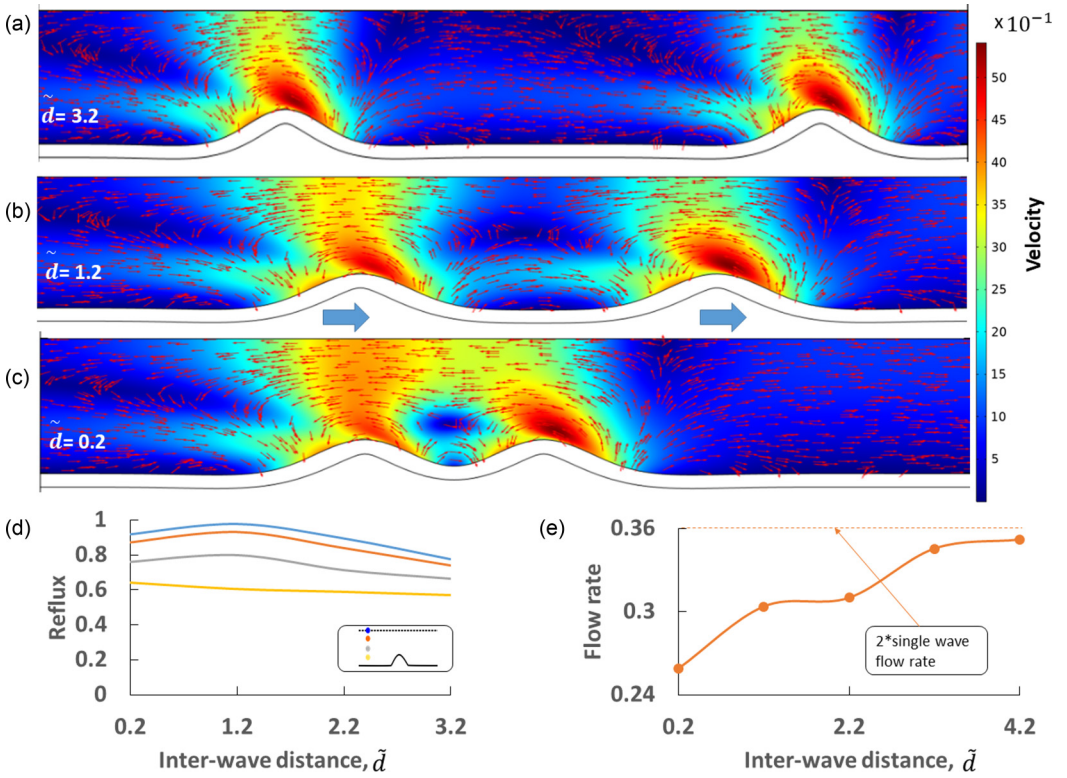

FIG. 6. Colinear train waves. 25% contractile wave amplitude (a) 3.2 interwave distance. (b) 1.2 interwave distance. (c) 0.2 interwave distance. (d) Reflux of four different particles at the same z position, different y positions. (e) Flow rate of two waves as a function of distance.

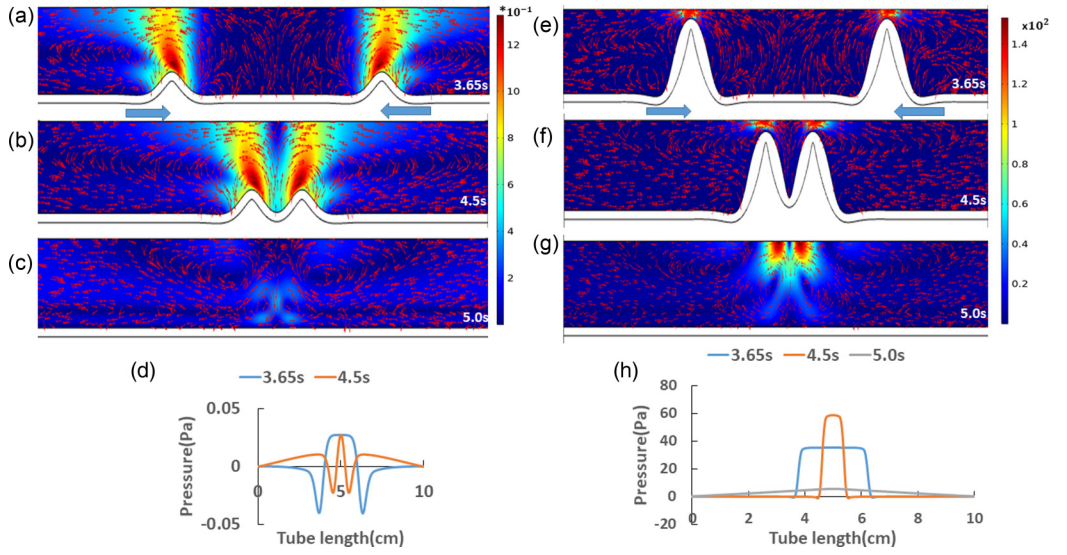

FIG. 7. Velocity profile and pressure of counterpropagating waves. Wave length 1, wave speed 1 and, 1×10^{-3} Pa s dynamic viscosity. (a)–(d) 25% contraction amplitude. (e)–(h) 88% contraction amplitude.

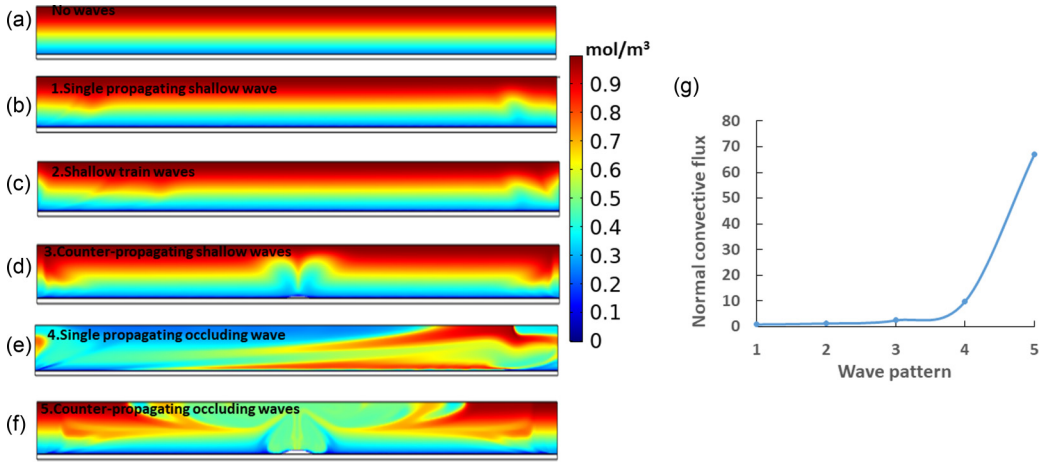

FIG. 8. Mixing of diluted species by different wave patterns. Wavelength = 1, speed = 1, dynamic viscosity 1 mPa s. For each wave pattern, two cycles were applied to the initial concentration profile shown in (a). (b)–(d) Shallow single propagating, colinear train(1.2 interwave separation) and counterpropagating waves of amplitude 25%. (e), (f) Occluding single and counterpropagating waves of amplitude 88%. (g) Convective flux of the different wave patterns (normalized by convective flux of single propagating shallow wave of amplitude 25%).

G. Mixing induced by different wave patterns

We finally studied how the different wave patterns—single waves of different amplitudes, colinear train waves, counterpropagating waves—mix intestinal fluid by examining the redistribution and absorption of an initially Gaussian concentration profile [Fig. 8(a)]. Shallow single [Fig. 8(b)] and train waves [Fig. 8(c)] did not give rise to any appreciable redistribution of solute and absorption [Fig. 8(g)]. In contrast, high-amplitude counterpropagating waves—Fig. 8(f), see the numerical simulation of counterpropagating waves, video S3, in Supplemental Material [23]—resulted in a significant deformation of the concentration profile at the point where the counterpropagating waves meet and annihilate as a result of the radial fluid velocity component arising during this event [Fig. 7(c)]. For high-amplitude (occluding) waves, both single unidirectional waves and counterpropagating waves gave rise to a significant amount of solute redistribution [Figs. 8(e) and 8(f)] and absorption [Fig. 8(c)]. Video S4 (see the numerical simulation of single propagating waves in the Supplemental Material [23]) shows that the ability of high-amplitude waves to induce mixing is due to the recirculating vortex upstream of the contraction [Fig. 3(c)].

IV. DISCUSSION

Motivated by the nonintuitive flow of bolus observed in our experimental setup (Fig. 2), we examined in this paper the flow characteristics of digesta under the action of a variety of different contraction patterns found in the gastrointestinal tract and in other smooth-muscle lined organs: single low- or high-amplitude waves, colinear train waves, and counterpropagating waves. For single waves (Fig. 3), our FEM model revealed vortical flow forming upstream of the contraction for high-amplitude waves. We established an analytical model and compared the flow characteristics (Fig. 4) as a function of the contractile wave parameters: velocity, amplitude, wave length, and bolus viscosity, and studied particle trajectories (Fig. 5). We next examined colinear waves (Fig. 6), found that hydrodynamics is the result of a nonlinear interaction at a small enough interwave distance [Fig. 6(e)], and that bolus reflux is maximized at a given interwave distance [Fig. 6(d)]. For counterpropagating waves (Fig. 7), our FEM simulation revealed that pressure in the region

between the two contractions increases as the waves get closer together, giving rise to high-velocity flow exiting this high pressure area. We finally found by examining redistribution of a solute inside the gut (Fig. 8) that both high-amplitude single waves and counterpropagating waves gave rise to considerable mixing of the bolus.

Our analytical and numerical findings rationalize the experimental observations presented in Fig. 2. For unidirectional, low-amplitude waves [Fig. 2(a)], we observed that the liquid bolus has a characteristic sawtooth dynamics [Fig. 2(b)], which is exactly what is predicted by computing the trajectory of a small particle submitted to a propagative, unidirectional wave [Fig. 5(b)]. Quantitatively, we measured experimental antegrade and retrograde velocities of 0.26 ± 0.05 and -2.2 ± 0.5, respectively [Fig. 2(b)]. Inputting the experimental parameters of the wave seen in Figs. 2(a) and 2(b) in our numerical (FEM) model predicts antegrade and retrograde velocities of 0.3 ± 0.1 and -1.7 ± 0.3, respectively, consistent with experimental results. When the size of the particle exceeds the size of the constricted lumen, the particle is transported unidirectionally at the same speed as that of the contractile wave, as predicted by our simulation [Fig. 5(d)] and observed experimentally for oil droplets [Figs. 2(c) and 2(d), video S2 [23], initial phase before collision]. When the contractile waves collide, the bolus is ejected at 35 times the speed of the contractile waves [Figs. 2(c) and 2(d), video S2 [23], after collision]. Our simulations explain this behavior by showing that a high pressure region forms between the two contractile waves (Fig. 7), giving rise to high velocity fluid jets with a velocity in the range 1.2 cm/s—140 times the speed of the contractile wave. These two events, reflux by single unidirectional waves and jets resulting from colliding contractile waves, result in high local bolus velocity, which increases shear stress at the epithelium and favors absorption by reducing the effective size of the diffusion layer.

The simple Poiseuille analytical model we set up Eq. (9) captures the qualitative behavior of the output flow as a function of the wave parameters (Fig. 4). In particular, the output flow is independent of viscosity, increases linearly with wave speed and wave length, and increases linearly with wave amplitude for $A > 0.5$ (half of the lumen occluded). For $A < 0.5$, the waves are inefficient at transporting bolus ([Fig. 4(c)]. Quantitatively, the Poiseuille model yielded pressure differentials [Fig. 3(d)] that were 40–50 times lower than the ones predicted by the FEM model and output flows (Fig. 4) that were 6.6 times lower than the ones predicted by the FEM model. We explain this by the fact that (1) the analytical model neglects the pressure exerted on the fluid by the contraction, while this is taken into account in the numerical model via transmission of the force from the deformed wall to the fluid and (2) reflux has been shown to depend sharply on the exact shape of the contractile wave [13], and our numerical model is in this respect more physiologically faithful than the analytical rectangular tube indentation. From a practical point of view, the formula

$$Q = 6.6 \times \frac{c\pi (R-r)^2}{\left(1 + \left(\frac{r}{R}\right)^4 \left(\frac{L}{l}\right)\right)} \tag{13}$$

(with the factor 6.6 correcting for these limitations), can be used to predict the flow generated by any contractile wave given its amplitude, speed, and wave length.

For colinear train waves, we found that bolus reflux, i.e., the extent of bolus retrograde displacement during one wave cycle, was maximized for an interwave distance of 1.2, and was higher than that created by single (widely spaces) waves. We compiled the distance between successive myogenic waves from experimental studies in the proximal, middle, and distal colon of rabbit [28] and guinea pig [29] and found a value of 1.3 ± 0.15, which is close to the optimum for reflux we found. This result suggests that the interwave distance of myogenic contractile waves may be naturally selected to optimize reflux of the bolus to optimize absorption. We note that, physiologically, the frequency and amplitude of waves are generally inversely related. In the human colon, for example [30–32], high [>10 cycles per minute (cpm)], intermediate ($2-4$ cpm), and low frequency (<1 cpm) contractions have, respectively, a low, media,n and high amplitude. The high and intermediate frequency waves promote mixing and absorption, while the more seldom, high-amplitude waves propel and flush out contents.

By examining redistribution of a solute inside the gut (Fig. 8), we found that high-amplitude waves and counterpropagating waves gave rise to considerable mixing of the bolus. The mixing ability of high-amplitude waves is related to the formation of a vortex upstream of the contractions, which FEM simulations put in the limelight (Fig. 3(c), video S4 [23]). Low-amplitude unidirectional waves, which do not generate vortical flow, do not induce mixing. The mixing ability of counterpropagating waves [17,28] is both due to the high velocity jet exiting the region that is compressed between the two waves and also to a radial velocity component arising when the two waves annihilate [29] (Figs. 7 and 8, video S3 [23]). Our simulations reveal the hydrodynamics behind the segmentation motor pattern, which is characterized by the generation of numerous counterpropagating waves along whole segments of the intestine [12], and whose physiological role is to promote mixing and absorption.

Qualitative and preliminary quantitative comparison of experimental and numerical data shows good agreement. One limitation of our study is that we did not systematically vary experimental parameters to the same extent than we did for the FEM model. We also only considered the effect of circular contractions, i.e., we did not include the effects of the longitudinal muscle layer. Rhythmic, nonpropagative activity of the longitudinal muscle results in pendular activity, which has been shown to accelerate mixing and the effective diffusion flux of nutrient to the epithelium [4]. We surmise that longitudinal pendular activity together with counterpropagating wave provides an optimal regime for bolus mixing and absorption.

Different wave patterns exist in different organs depending on the function of the organs. We have shown that the gut produces shallow train waves to ensure redistribution, reflux, and delay bolus transit time. Widely spaced waves are more efficient at continuous pumping than train waves and high amplitude contractile waves are well adapted for clearing contents, or mixing if they are counterpropagating. Organs like the ureter and esophagus, where mixing and absorption are not necessary, employ lumen obliterating unidirectional waves. Counterpropagating waves are efficient at mixing, creating vortices, and recirculation zones that ensure that all parts of the chyme come in contact with the wall of the gut for absorption.

ACKNOWLEDGMENTS

The authors thank the animal husbandry staff of Institut Jacques Monod for providing embryonic mice and acknowledge the generous support from the IDEX Université de Paris Grant No. ANR-18-IDEX-0001 and from the Agence Nationale de la Recherche Projet-ANR-19-CE30-0016.

[1] J. Huizinga and W. Lammers, Gut peristalsis is governed by a multitude of cooperating mechanisms, Am. J. Physiol.-Gastrointestinal Liver Physiol. **296**, G1 (2009).

[2] H. Maia and E. Coutinho, Peristalsis and antiperistalsis of the human fallopian tube during the menstrual cycle, Biol. Reprod. **2**, 305 (1970).

[3] D. Griffiths, Flow of urine through the ureter: A collapsible, muscular tube undergoing peristalsis, J. Biomech. Eng. **111**, 206 (1989).

[4] C. de Loubens, R. Lentle, R. Love, C. Hulls, and P. Janssen, Fluid mechanical consequences of pendular activity, segmentation and pyloric outflow in the proximal duodenum of the rat and the guinea pig, J. R. Soc. Interface **10**, 20130027 (2013).

[5] P. Janssen, R. G. Lentle, P. Asvarujanon, P. Chambers, K. J. Stafford, and Y. Hemar, Characterization of flow and mixing regimes within the ileum of the brushtail possum using residence time distribution analysis with simultaneous spatio-temporal mapping, J. Physiol. **582**, 1239 (2007).

[6] B. Jeffrey, H. Udaykumar, and K. Schulze, Flow fields generated by peristaltic reflex in isolated guinea pig ileum: Impact of contraction depth and shoulders, Am. J. Physiol.-Gastrointestinal Liver Physiol. **285**, G907 (2003).

[7] R. J. Love, R. G. Lentle, P. Asvarujanon, and Y. Hemar, An expanded finite element model of the intestinal mixing of digesta, Food Dig. **4**, 26 (2013).
[8] K. Nikaki, A. Sawada, and A. Ustaoglu, Neuronal control of esophageal peristalsis and its role in esophageal disease, Curr. Gastroenterol Rep. **21**, 59 (2019).
[9] F. Kiil, *Urinary Flow and Ureteral Peristalsis* (Springer, Berlin, 1973).
[10] J. E. Richter, W. C. Wu, D. N. Johns, J. N. Blackwell, J. L. Nelson III, J. A. Castell, and D. O. Castell, Esophageal manometry in 95 healthy adult volunteers. variability of pressures with age and frequency of abnormal contractions, Digest Dis Sci **32**, 583 (1987).
[11] N. Spencer, P. Dinning, S. Brookes, and M. Costa, Insights into the mechanisms underlying colonic motor patterns, J. Physiol. **594**, 4099 (2016).
[12] J. D. Huizinga, J. H. Chen, Y. F. Zhu, A. Pawelka, R. J. McGinn, B. L. Bardakjian, S. P. Parsons, W. A. Kunze, R. Y. Wu, P. Bercik, A. Khoshdel, S. Chen, S. Yin, Q. Zhang, Y. Yu, Q. Gao, K. Li, X. Hu, N. Zarate, P. Collins, M. Pistilli, J. Ma, R. Zhang, and D. Chen, The origin of segmentation motor activity in the intestine, Nat. Commun. **5**, 3326 (2014).
[13] M. Li and J. Brasseur, Non-steady peristaltic transport in finite-length tubes, J. Fluid Mech. **248**, 129 (1993).
[14] A. H. Shapiro, M. Y. Jaffrin, and S. L. Weinberg, Peristaltic pumping with longwavelength at low Reynolds number, J. Fluid Mech. **37**, 799 (1969).
[15] R. Gwynne, E. Thomas, S. Goh, H. Sjovall, and J. Bornstein, Segmentation induced by intraluminal fatty acid in isolated guinea-pig duodenum and jejunum, J. Physiol. **556**, 557 (2004).
[16] M. Sinnott, P. Cleary, J. Arkwright, and P. Dinning, Investigating the relationships between peristaltic contraction and fluid transport in the human colon using smoothed particle hydrodynamics, Comput. Biol. Medicine **42**, 492 (2012).
[17] N. R. Chevalier, The first digestive movements in the embryo are mediated by mechanosensitive smooth muscle calcium waves, Philos. Trans. R. Soc. London B **373**, 20170322 (2018).
[18] C. de Loubens, R. G. Lentle, C. Hulls, P. W. M. Janssen, R. J. Love, and J. P. Chambers, Characterisation of mixing in the proximal duodenum of the rat during longitudinal contractions and comparison with a fluid mechanical model based on spatiotemporal motility data, PLoS One **9**, e95000 (2014).
[19] K. S. Schulze and E. Clark, Ink dispersion by sequential contractions in isolated segments of guinea pig ileum and duodenum, Neurogastroenterol Motil. **20**, 1317 (2008).
[20] J. Zha, S. Zou, J. Hao, X. Liu, G. Delaplace, R. Jeantet, D. Dupont, P. Wu, X. D. Chen, and J. Xiao, The role of circular folds in mixing intensification in the small intestine: A numerical study, Chem. Eng. Sci. **229**, 116079 (2021).
[21] R. Roberts, M. Ellis, R. M. Gwynne, A. J. Bergner, M. D. Lewis, E. A. Beckett, J. C. Bornstein, and H. M. Young, The first intestinal motility patterns in fetal mice are not mediated by neurons or interstitial cells of cajal, J. Physiol. **588**, 1153 (2010).
[22] N. Chevalier, Y. Ammouche, C. Teyssaire, P. de Santa Barbara, and S. Faure, Shifting into high gear: how interstitial cells of cajal change the motility pattern of the developing intestine, Am. J. Physiol.-Gastrointestinal Liver Physiol. **319**, G519 (2020).
[23] See Supplemental Material at http://link.aps.org/supplemental/10.1103/PhysRevFluids.7.043101 for the bolus dynamics of meconium in the hindgut of a mouse, oil displacement by counterpropagating waves of embryonic chicken, numerical solute redistribution by different wave patterns, rheological properties of gastrointestinal organs, and reflux as a function amplitude of wave contraction [33].
[24] N. R. Chevalier, N. Dacher, C. Jacques, L. Langlois, C. Guedj, and O. Faklaris, Embryogenesis of the peristaltic reflex, J. Physiol. **597**, 2785 (2019).
[25] N. Chevalier, V. Fleury, S. Dufour, V. Proux-Gillardeaux, and A. Asnacios, Emergence and development of gut motility in the chicken embryo, PLoS One **12**, e0172511 (2017).
[26] C. Renaud, J.-M. Cros, Z.-Q. Feng, and B. Yang, The Yeoh model applied to the modeling of large deformation contact/impact problems, Int. J. Impact Eng. **36**, 659 (2009).
[27] G. D'Antona, G. Hennig, M. Costa, C. M. Humphreys, and S. J. Brookes, Analysis of motor patterns in the isolated guinea-pig large intestine by spatio-temporal maps, Neurogastroenterol. Motil. **13**, 483 (2001).

[28] P. Dinning, M. Costa, S. Brookes, and N. Spencer, Neurogenic and myogenic motor patterns of rabbit proximal, mid, and distal colon, Am. J. Physiol.-Gastrointestinal Liver Physiol.y **303**, G83 (2012).
[29] G. Hennig, S. Gregory, S. Brookes, and M. Costa, Non-peristaltic patterns of motor activity in the guinea-pig proximal colon, Neurogastroenterol. Motil. **22**, e207 (2010).
[30] P. Bampton, P. G. Dinning, M. L. Kennedy, D. Z. Lubowski, D. deCarle, and I. J. Cook, Spatial and temporal organization of pressure patterns throughout the unprepared colon during spontaneous defecation, Am. J. Gastroenterol. **95**, 1027 (2000).
[31] I. Cook, Y. Furukawa, V. Panagopoulos, P. J. Collins, and J. Dent, Relationships between spatial patterns of colonic pressure and individual movements of content, Am. J. Physiol.-Gastrointestinal Liver Physiol. **278**, G329 (2000).
[32] S. Rao, P. Sadeghi, J. Beaty, R. Kavlock, and K. Ackerson, Ambulatory 24-h colonic manometry in healthy humans, Am. J. Physiol.-Gastrointestinal Liver Physiol. **280**, G629 (2001).
[33] R. K. Avvari, in *Digestive System*, edited by X. Qi and S. Koruth (IntechOpen, Rijeka, 2020), Chap. 4.